INSTITUTE OF PHYSICS PUBLISHING JOURNAL OF PHYSICS D: APPLIED PHYSICS

J. Phys. D: Appl. Phys. **38** (2005) 1805–1823 doi:10.1088/0022-3727/38/11/021

Large-scale molecular dynamics simulation of surface nanostructuring with a laser-assisted scanning tunnelling microscope

Xinwei Wang

Department of Mechanical Engineering, The University of Nebraska-Lincoln, N104 Walter Scott Engineering Center, Lincoln, NE 68588-0656, USA

E-mail: xwang3@unl.edu

Received 24 December 2004, in final form 15 February 2005
Published 20 May 2005
Online at stacks.iop.org/JPhysD/38/1805

Abstract

In this work, large-scale molecular dynamics simulations are conducted to explore the thermal and mechanical phenomena in surface nanostructuring with a laser-assisted scanning tunnelling microscope. Employing a super parallel computer, more than 200 million atoms are modelled to provide substantial details about how the localized thermal and mechanical perturbations result in surface nanostructures. Extremely localized stress accumulation beneath the sample surface leads to an explosion of the melted/vaporized material, leaving a nanoscale hole in the sample surface. Normal and shear stress development are observed. Stress propagation in space is strongly influenced by the anisotropic nature of the crystal. The high pressure in the melted/vaporized region pushes the melt adjacent to the solid to move, thereby forming a protrusion at the edge of the hole. More importantly, visible sub-surface nanoscale structural damages are observed in a direction 45° with respect to the axial direction. Detailed study of the lattice structure reveals atomic dislocations in the damaged regions. Both temporary and permanent structural damages are observed in the material. The temporary structural damage is featured with a formation, propagation and disappearing procedure.

1. Introduction

In a laser-assisted scanning tunnelling microscope (STM) there are various ways in which the laser beam is integrated with the STM. For instance, the laser could be used to irradiate the sample surface to generate a photovoltage [1, 2], to result in thermal expansion [3], or to excite photoelectrons [4]. In this paper, laser-assisted STM refers to the case when the STM tip is irradiated with a laser beam. In the past several years, extensive research has been conducted to explore mechanisms of laser-assisted STM surface nanostructuring [5, 6]. These mechanisms can be roughly classified into five categories. First, the STM tip undergoes a thermal expansion upon pulsed laser irradiation, resulting in mechanical contact with the sample surface to form nano-indentations [7–13]. Second, the STM tip could act as a receiving antenna to collect laser energy and as a transmitting antenna to create a significantly enhanced optical field in proximity to the tip apex. The optical field could be enhanced by two orders of magnitude [14]. Therefore, the enhanced optical field can heat the sample surface to induce phase change or a chemical reaction and modify the surface at nanoscales [7, 12, 13, 15–22]. In the work by Chimmalgi *et al* [21] and Huang *et al* [22], a laser-assisted atomic force microscope (AFM) was used, which plays the same role as the laser-assisted STM in terms of optical field enhancement. Third,

when the STM tip thermally expands, the gap between the tip and the sample surface will reduce, resulting in a substantial increase in the tunnelling current (when the tip is biased during laser irradiation) [23–25]. This increased tunnelling current could stimulate chemical adsorption of atoms from the sample surface, thereby achieving nanostructuring [26]. Fourth, upon pulsed laser heating, the temperature of the STM tip will increase substantially, making atoms escape from the apex of the tip. In addition, due to the thermal expansion of the tip, the tip will approach the sample surface to result in enhanced interaction with the sample surface. As a collective result of these two mechanisms, atoms can be transferred from the tip to the sample surface to form nanostructures [27]. Finally, the pulsed laser can dissociate gas species between the tip and the sample surface to free individual atoms. The electric field between the tip and the sample surface then deposits these atoms on the sample surface to form nanohillocks [28, 29]. It is worth noting that in practical laser-assisted STM nanomanufacturing, several of these mechanisms could co-exist to attain the final surface nanomodification. Comprehensive and detailed information on laser-assisted STM can be found in a recent review by Grafström [6].

Despite the significant amount of research on laser-assisted STM surface nanostructuring, the extent of the contribution of each mechanism in determining the final surface nanostructure is still not clear. Furthermore, it is observed that the final surface nanostructures/patterns showed appreciable irregularities, which were evident in a large number of reports [11–13, 16, 26]. A quantitative understanding of the role of each mechanism in laser-assisted STM nanostructuring is critical in terms of manipulating the manufacturing process to achieve neat nanostructures with molecular/atomic level precision. Among the mechanisms outlined above, sample heating by the enhanced optical field and mechanical contact between the tip and the sample surface play prominent roles in laser-assisted STM surface nanostructuring [8–13, 17–20, 22]. In these two mechanisms, the sample surface experiences extremely localized thermal excitation and mechanical perturbation. Little information has been obtained on the thermal and mechanical behaviour of the sample under these nanoscale thermal and mechanical influences. Although a large number of calculations have been reported on the enhanced optical field [30–34], only the temperature field of the sample surface under the enhanced optical field has been studied to a limited extent [35, 36].

At nanoscales, thermal movements of molecules/atoms will show strong statistical variations in space since thermal equilibrium cannot be established. Therefore, continuum approaches will fail to predict the thermal and thermally induced behaviour of the sample. Molecular dynamics (MD) simulations, which directly track the movement of molecules/atoms, are capable of exploring physical phenomena down to molecular/atomic levels. In the past, MD simulations have been used for years to study laser–material interaction. Shibahara and Kotake [37, 38] studied the interaction between metallic atoms and a laser beam in a system consisting of 13 or fewer atoms. Their work focused on the structural change of metallic atoms due to laser beam absorption. Häkkinen and Landman [39] studied the dynamics of superheating, melting and annealing at the Cu surface induced by laser beam irradiation. Kotake and Kuroki [40] studied the laser ablation of a small dielectric system. In their work, laser beam absorption was simulated by exciting the potential energy of atoms. Applying the same laser beam absorption approach, Herrmann *et al* [41] investigated laser ablation of a silicon crystal containing approximately 23 000 atoms. Zhigilei *et al* [42, 43] studied the laser induced ablation of organic solids using the breathing sphere model, which approximated laser irradiation by exciting the molecular vibration. Their work revealed a number of physical phenomena in picosecond laser organic material interaction, which can be found in a recent paper and the references cited in [44]. For laser–metal interaction, different techniques have been employed to consider thermal transport by electrons, which cannot be accounted for within classical MD schemes. Examples include forced heat

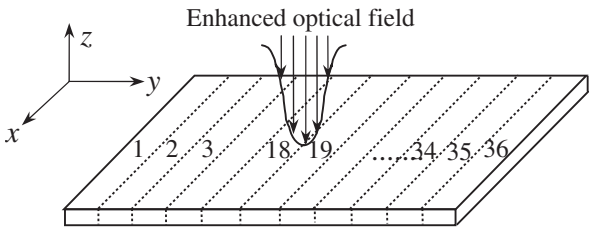

Figure 1. Schematic of the MD configuration.

Table 1. Values of the parameters used in the simulation.

Parameter	Value
ε, LJ well depth parameter	1.653×10^{-21} J
σ_e, LJ equilibrium separation	3.406 Å
m, Argon atomic mass	66.3×10^{-27} kg
k_B, Boltzmann's constant	1.38×10^{-23} J K^{-1}
a, Lattice constant	5.414 Å
r_c, Cut off distance	8.515 Å
τ, Laser beam absorption depth	10 nm
δt, Time step	25 fs
I_0	1.5325×10^{12} W m^{-2}
r_g	25 nm
t_0	10 ps
t_g	3 ps

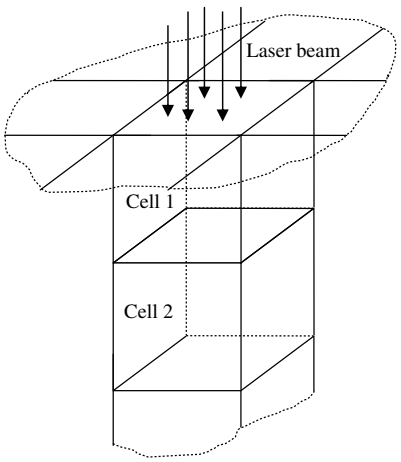

Figure 2. Schematic of the laser beam absorption in the material.

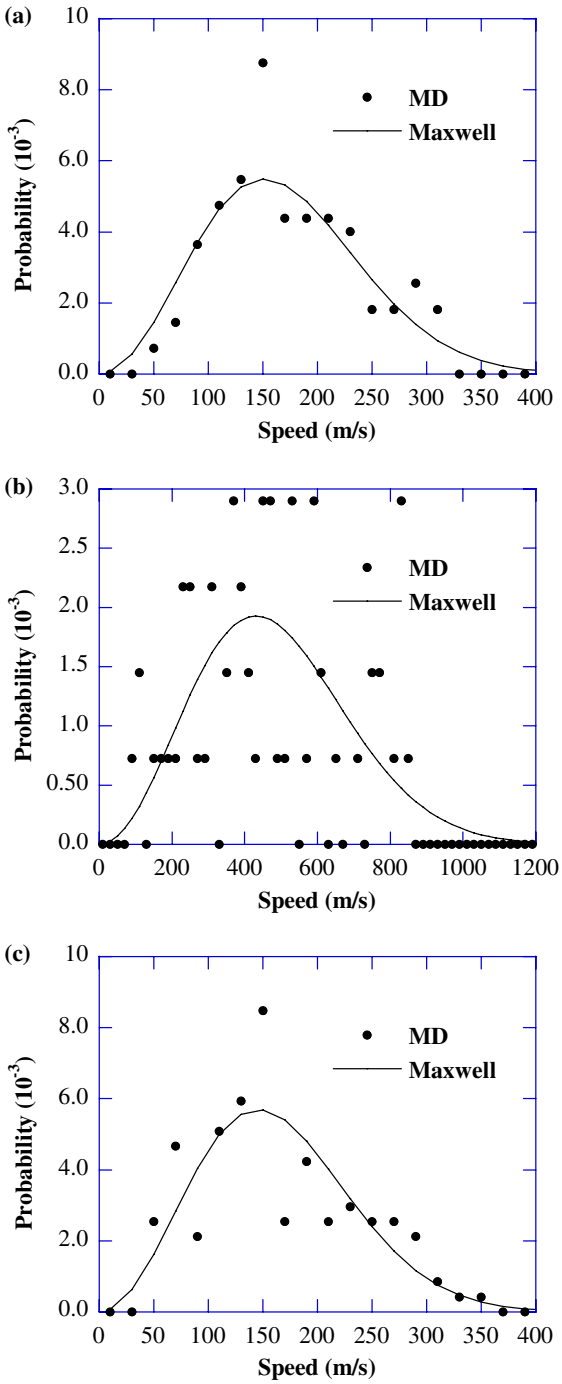

Figure 3. Velocity distribution of atoms within a domain of 1.77 nm size centred at $x = 174.56$ nm, $y = 174.53$ nm and $z = 245.33$ nm. (*a*) Before laser heating ($t = 5$ ps) and (*b*) after laser heating ($t = 15$ ps). For comparison, (*c*) shows the velocity distribution of a domain of the same size but far from the heating region ($x = 349.12$ nm, $y = 174.53$ nm and $z = 242.78$ nm, $t = 15$ ps).

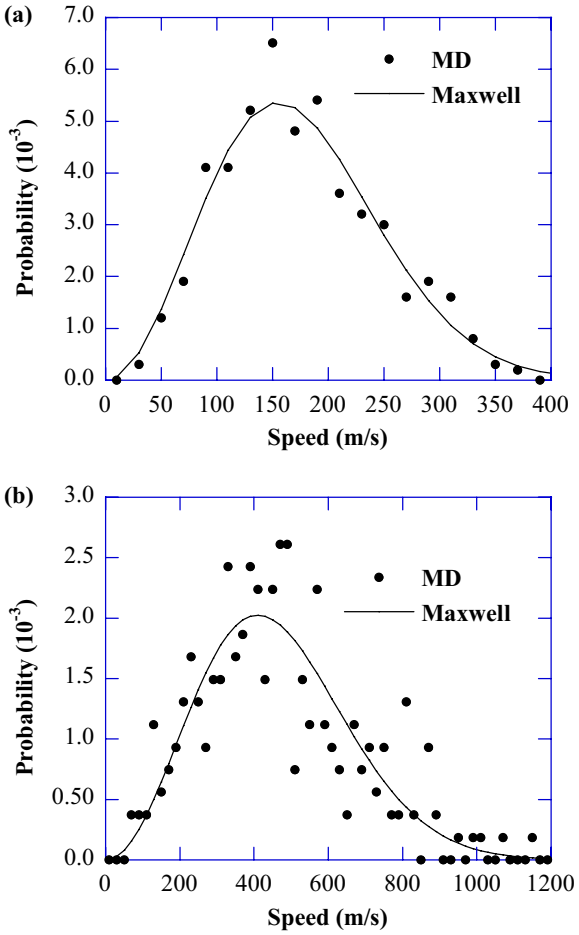

Figure 4. Velocity distribution of atoms within a domain of 1.77 nm in the y and z directions, and 6.81 nm in the x direction. The centre of the domain is located at $x = 174.56$ nm, $y = 174.53$ nm and $z = 245.33$ nm. (*a*) Before laser heating ($t = 5$ ps) and (*b*) after laser heating ($t = 15$ ps).

conduction among atoms [45] and the two-step heat transfer model [39, 46–48]. The mechanical wave in laser–material interaction in a large system was studied by Etcheverry and Mesaros [49]. In recent years, thermal transport, phase change, thermal stress development and propagation, and nanoparticle formation in laser–material interaction have been extensively investigated by the author [50–52]. Despite the research reviewed above, little MD simulation has been conducted to explore thermally induced stress/strain and structural damages in laser-assisted STM nanostructuring, which requires a much larger simulation domain to address the underlying physics.

In this work, large-scale parallel MD programs are developed to explore the thermal transport, stress development and propagation, and sub-surface nanoscale structural damages in surface nanostructuring with laser-assisted STM. Large size MD domains consisting of more than 200 million atoms are modelled to capture details of these nanoscale phenomena. The research is focused on the interaction of the sample with the enhanced optical field in laser-assisted STM. In section 2, methodologies of the simulation are introduced. Section 3 presents the results regarding the various thermal and mechanical behaviour of the sample, and section 4 summarizes the conclusion drawn from this work.

2. Methodologies of simulation

2.1. MD simulation

As delineated in figure 1, the MD simulation is intended to approximate a free-standing film irradiated with an enhanced

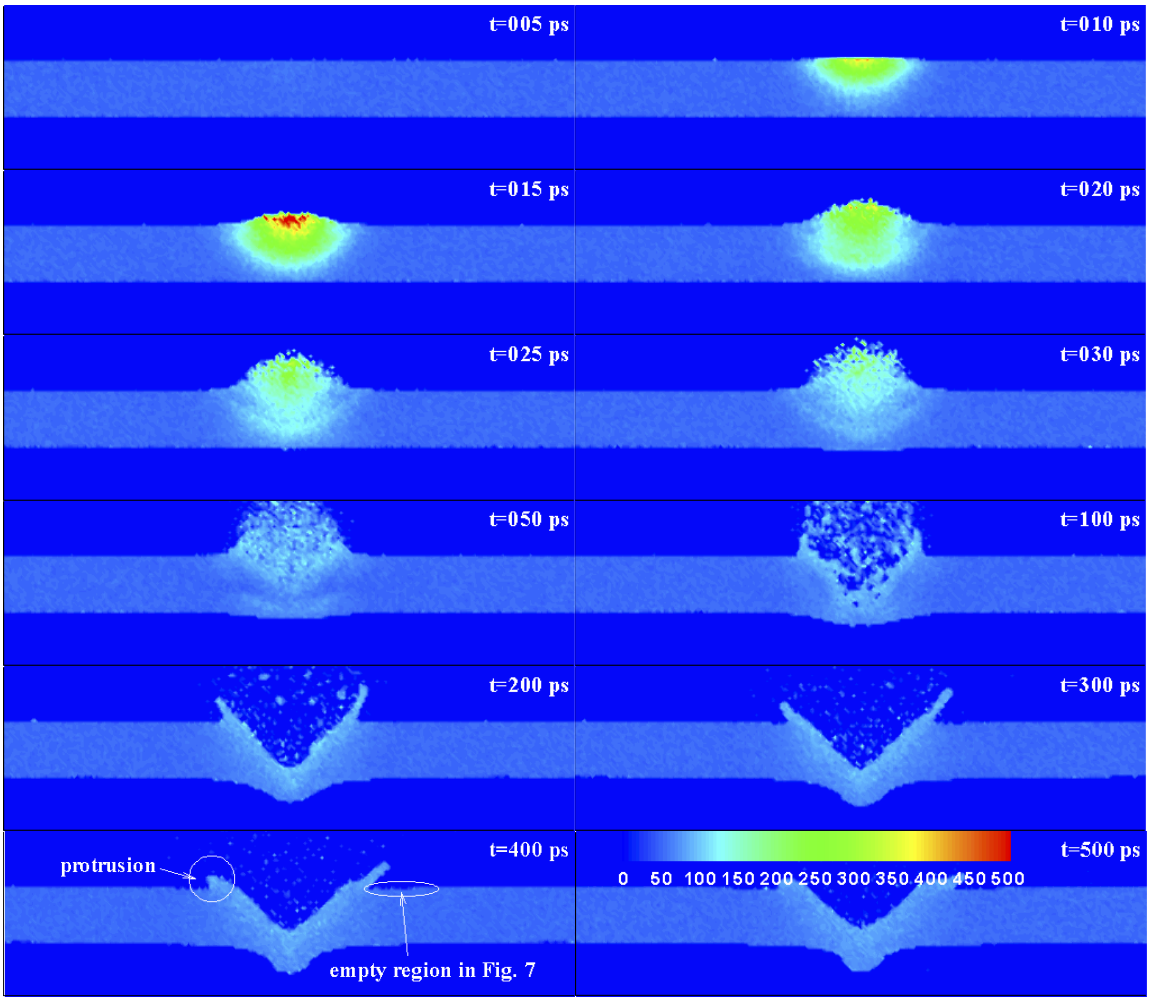

Figure 5. The temperature in an x (horizontal: 0–350 nm)–z (vertical: 180–280 nm) plane 1.77 nm thick centred at $y = 174.53$ nm.

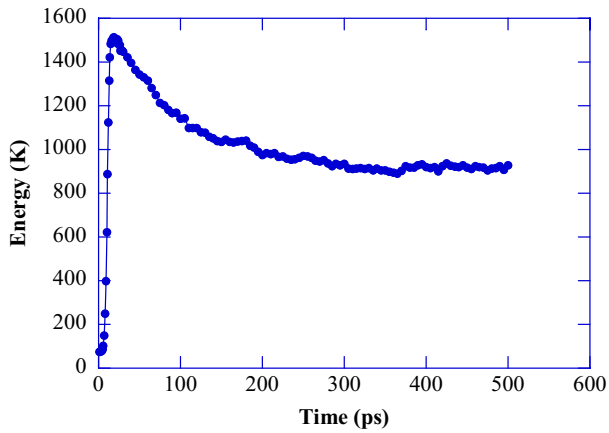

Figure 6. Evolution of the average kinetic energy of atoms originally located within a domain centred at $x = 175.414$ nm, $y = 175.414$ nm and $z = 244.057$ nm. The size of the domain is $\Delta x = 3.406$ nm, $\Delta y = 3.544$ nm and $\Delta z = 4.274$ nm. The kinetic energy is normalized with respect to k_B and is in the unit of Kelvin.

optical field. The film is assumed to be an argon crystal with an initial temperature of 50 K. In laser-assisted STM surface nanostructuring, the sample has to be conductive or semiconductive in order to make the STM applicable. However, in laser-assisted AFM nanomanufacturing, the sample can be either dielectric or metallic. As the first step to study the thermal and mechanical behaviour of materials in the nanostructuring process, argon is chosen as the material because of the simplicity of the MD simulation and the widely studied molecular potential of argon.

The movement of atoms is governed by the Newtonian equation,

$$m_i \frac{\mathrm{d}^2 r_i}{\mathrm{d}t^2} = \sum_{j \neq i} F_{ij}, \tag{1}$$

where m_i and r_i are the mass and position of atom i, respectively, and m_i is 6.63×10^{-26} kg for argon. F_{ij} is the interaction force between atoms i and j, and is computed from the Lennard–Jones (LJ) potential as $F_{ij} = -\partial\phi_{ij}/\partial r_{ij}$. The LJ potential ϕ_{ij} follows the form

$$\phi_{ij} = 4\varepsilon \left[\left(\frac{\sigma_e}{r_{ij}} \right)^{12} - \left(\frac{\sigma_e}{r_{ij}} \right)^{6} \right], \tag{2}$$

where ε is the LJ well depth parameter, and the corresponding value for argon is 1.653×10^{-21} J. σ_e is referred to as the equilibrium separation parameter (3.406 Å for argon), and $r_{ij} = r_i - r_j$.

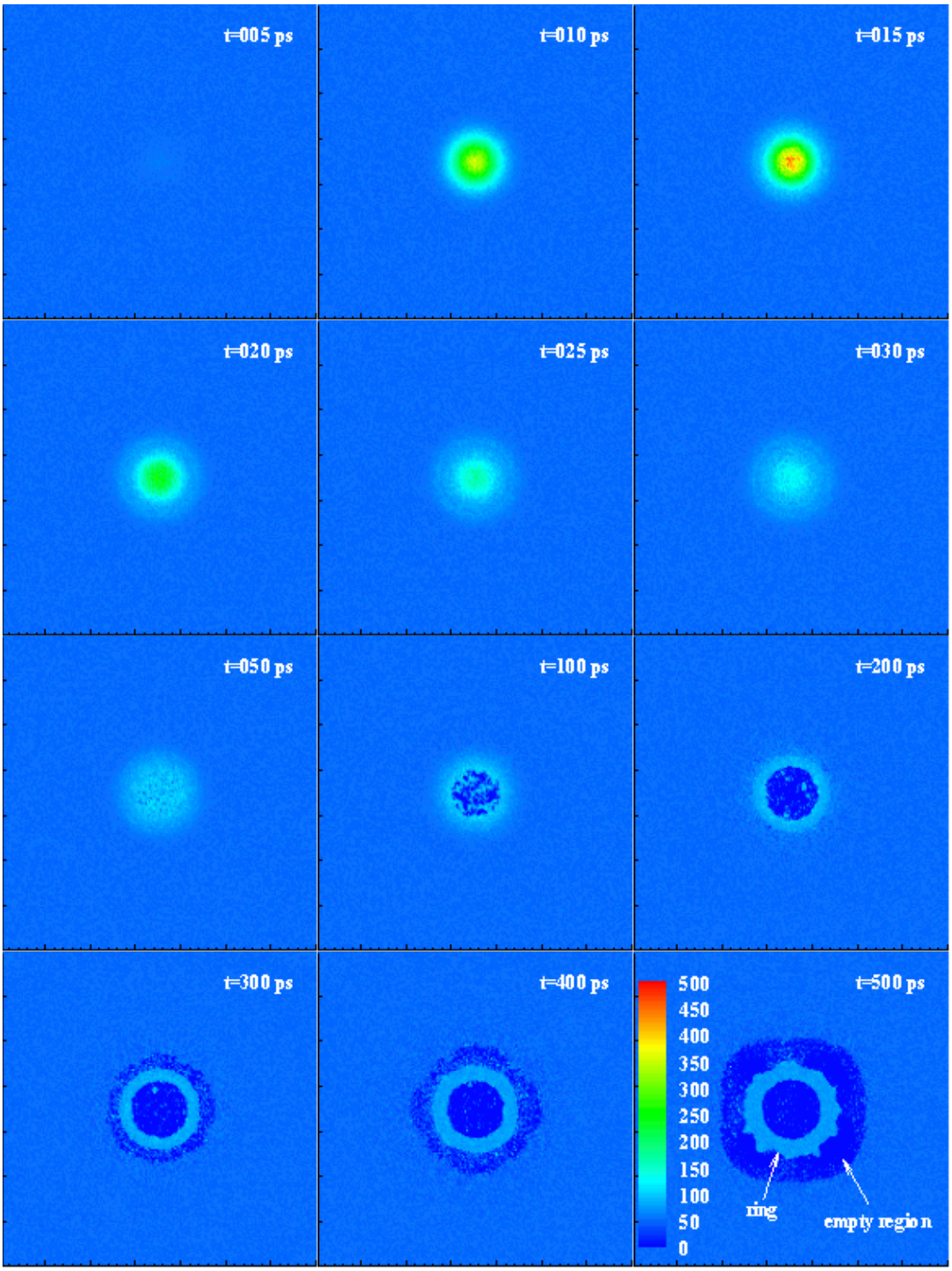

Figure 7. The temperature in an x (horizontal: 0–350 nm)–y (vertical: 0–350 nm) plane 1.71 nm thick centred at $z = 245.34$ nm.

Equation (1) is solved using the half-step leap-frog scheme—a modification to the velocity Verlet algorithm [53]. A time step of 25 fs is applied in the simulation. The interaction between atoms is neglected when their distance exceeds a particular length r_c, namely, the cutoff distance. For argon, the widely accepted value of $2.5\sigma_e$ for r_c is adopted. Computation of the force between an atom and its neighbours is arranged by the cell structure and linked-list methods [53]. More details about the computation can be found in the work by Wang and Xu [50].

Parallel computation is employed in this work. In the y direction, the physical domain is divided into 36 sub-domains of the same size as shown in figure 1. These sub-domains are distributed over a super-parallel computer consisting of a cluster of 36 computing points. Each computing point is responsible for the MD simulation of one sub-domain.

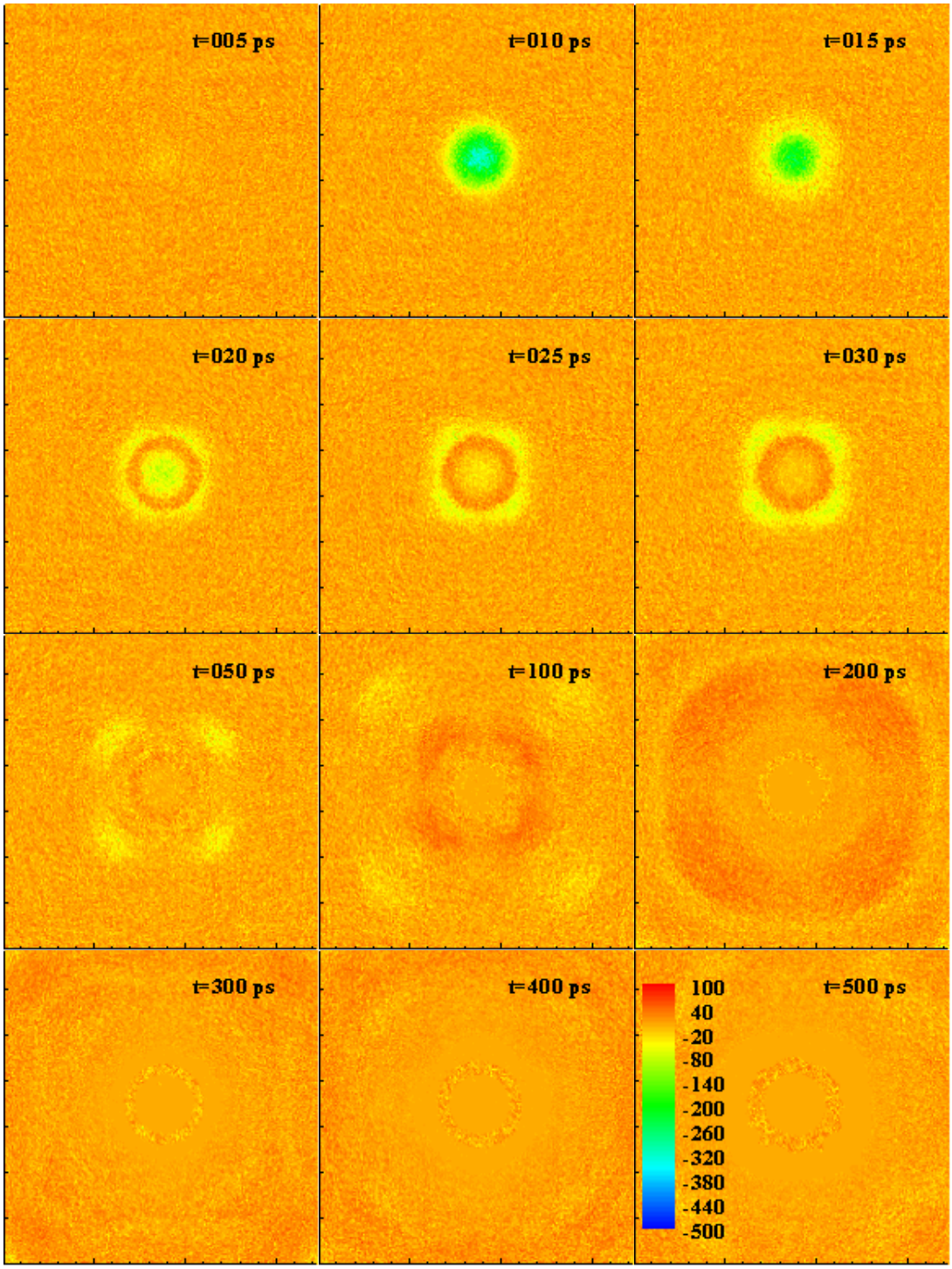

Figure 8. The stress σ_{rr} (MPa) in an x (horizontal: 0–350 nm)–y (vertical: 0–350 nm) plane 1.71 nm thick centred at $z = 245.34$ nm.

The parallel program is developed using MPICH, which is a portable implementation of MPI (message-passing-interface). Each sub-domain needs information about the position of atoms adjacent to it for force computation. In addition, during the computation, some atoms will leave one sub-domain and enter another one. All this information exchange among sub-domains is realized using data exchange among them through a dedicated fast local network. Details of the parallel treatments are discussed in our recent work [54].

2.2. Laser beam absorption

The distribution of the optical field in space and time domains is expressed as

$$I = I_0 \cdot \exp\left(-\frac{(\vec{r} - \vec{r}_0)^2}{r_g^2}\right) \cdot \exp\left(-\frac{(t - t_0)^2}{t_g^2}\right), \quad (3)$$

where I_0 is a laser beam intensity constant, $\vec{r}$ is the location of the laser beam, $\vec{r}_0$ is the centre of the sample surface, r_g is

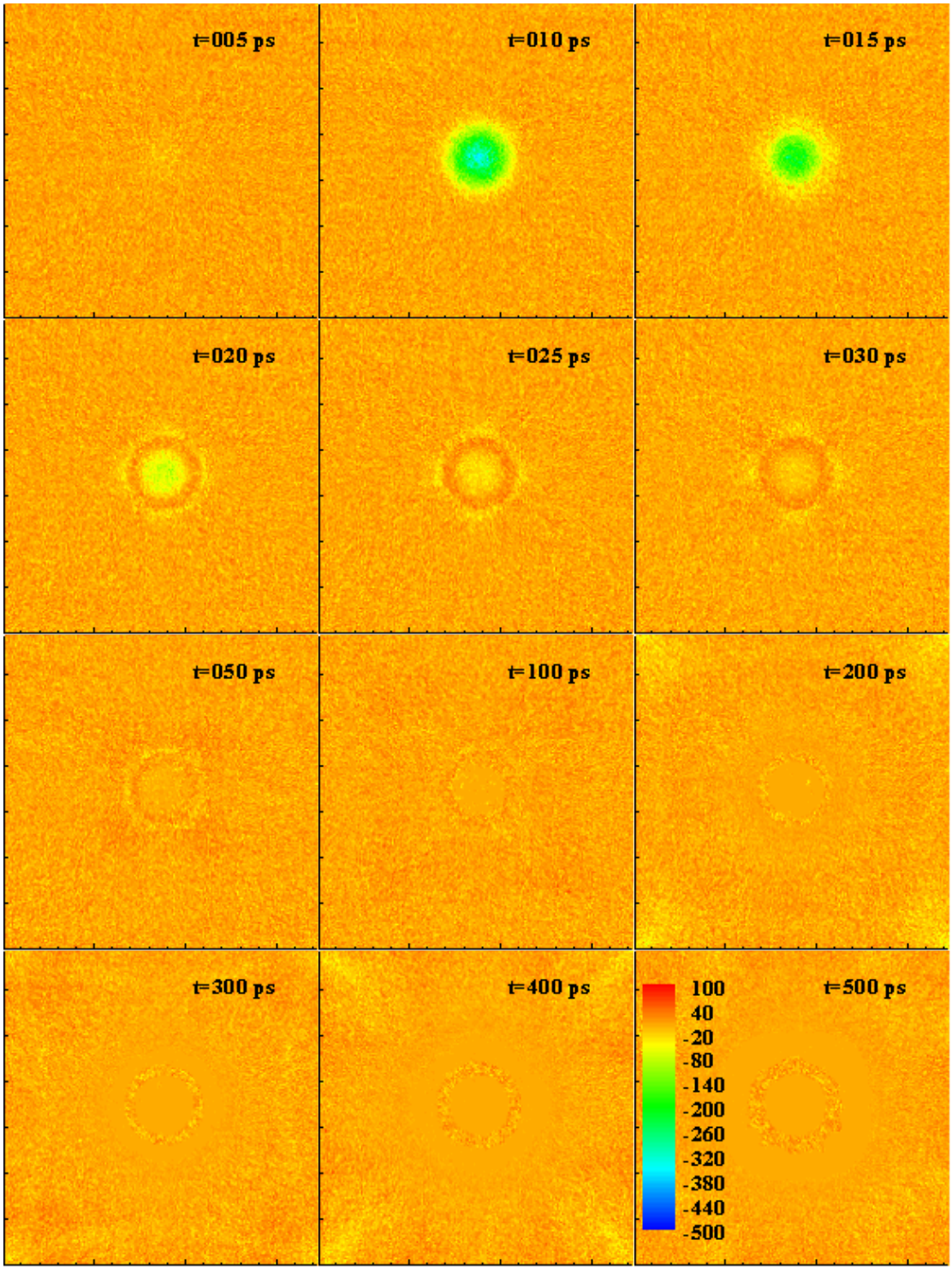

Figure 9. The stress $\sigma_{\theta\theta}$ (MPa) in an x (horizontal: 0–350 nm)–y (vertical: 0–350 nm) plane 1.71 nm thick centred at $z = 245.34$ nm.

a length constant determining the size of the laser beam, t is the time, t_0 is a time constant determining the peak location of the laser intensity in the time domain, and t_g is a time constant determining the pulse width of the laser beam. The laser beam distribution in equation (3) is constructed for the convenience of computing. Values of these parameters are summarized in table 1. The full-width at half-maximum (FWHM) of the laser pulse is 5 ps centred at 10 ps (1 ps $= 10^{-12}$ s). The light is exponentially absorbed in the film with an artificial optical absorption depth (τ) of 10 nm. This optical absorption depth is chosen to reflect the fact of volumetric absorption of the laser beam in the sample rather than to represent a practical experimental condition.

Figure 2 shows how the laser energy is absorbed in the material. As mentioned above, the linked-list method is used in the MD simulation. The MD domain is divided into small cubic

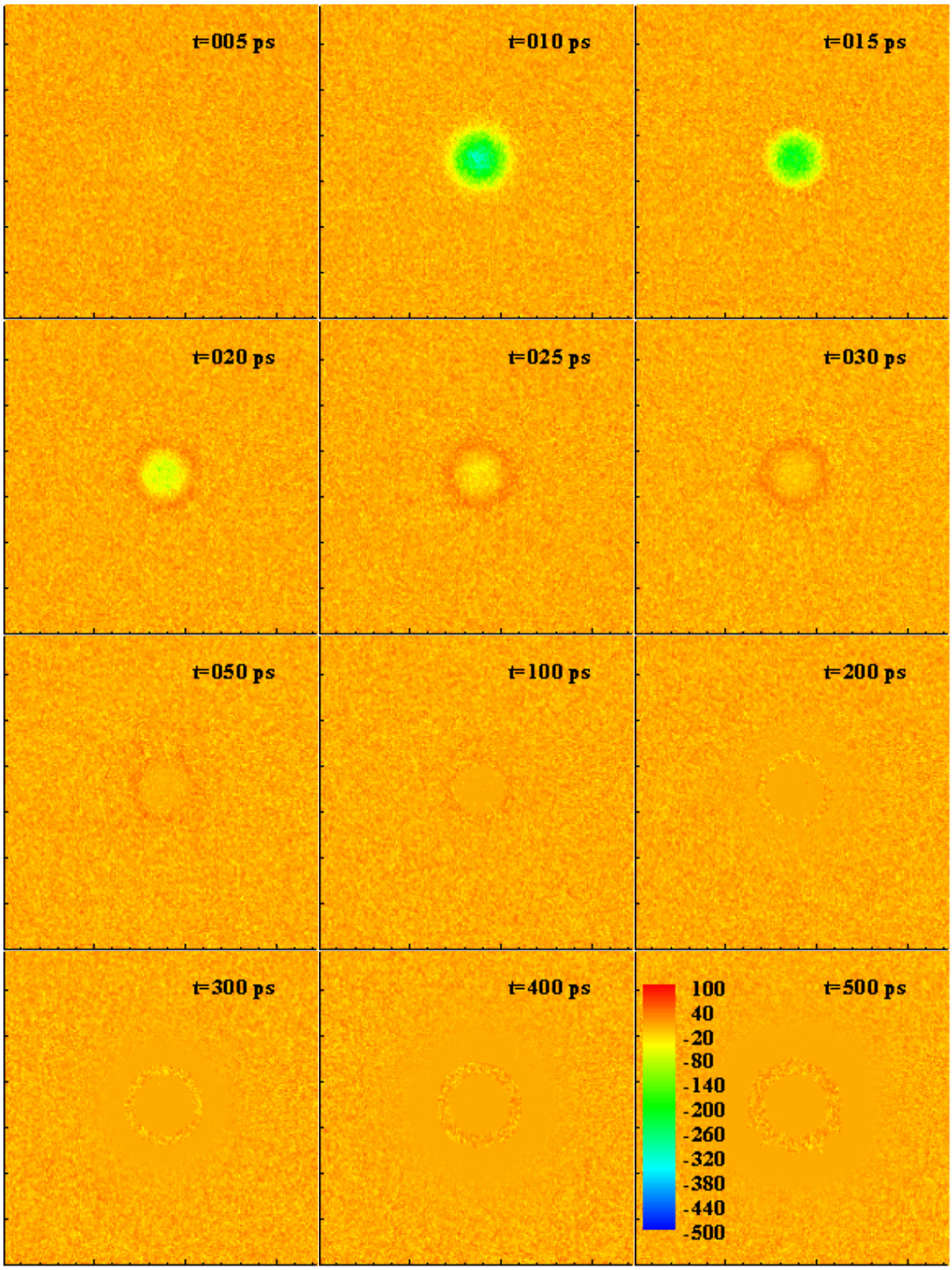

Figure 10. The stress σ_{zz} (MPa) in an x (horizontal: 0–350 nm)–y (vertical: 0–350 nm) plane 1.71 nm thick centred at $z = 245.34$ nm.

cells, whose size is a little larger than the cutoff distance. Cell 1 is the first cell in the laser-incident direction. In our calculation, this cell will be far above the target. The laser energy incident on cell 1 within each time step (δt) will be $E_1 = \int_A I\delta t \cdot \mathrm{d}A$ where A is the top surface of cell 1. At each time step, the density of atoms within cell 1 will be calculated to be ρ_1. The assumed absorption depth ($\tau = 10$ nm) is for the argon crystal at 50 K, whose density is designated as ρ_0. Since the density of cell 1 (ρ_1) can deviate from ρ_0, due to heating, explosion and other physical processes, the real optical absorption depth of cell 1 is adjusted to be $\tau_1 = \tau \cdot \rho_0/\rho_1$. Therefore, the laser energy absorbed by atoms in cell 1 within each time step is

$$\delta E_1 = E_1 \cdot \left(1 - \exp\left(-\frac{\delta z}{\tau_1}\right)\right), \tag{4}$$

where δz is the size of cell 1 in the z direction. This laser beam absorption is achieved by adjusting the velocity of atoms in

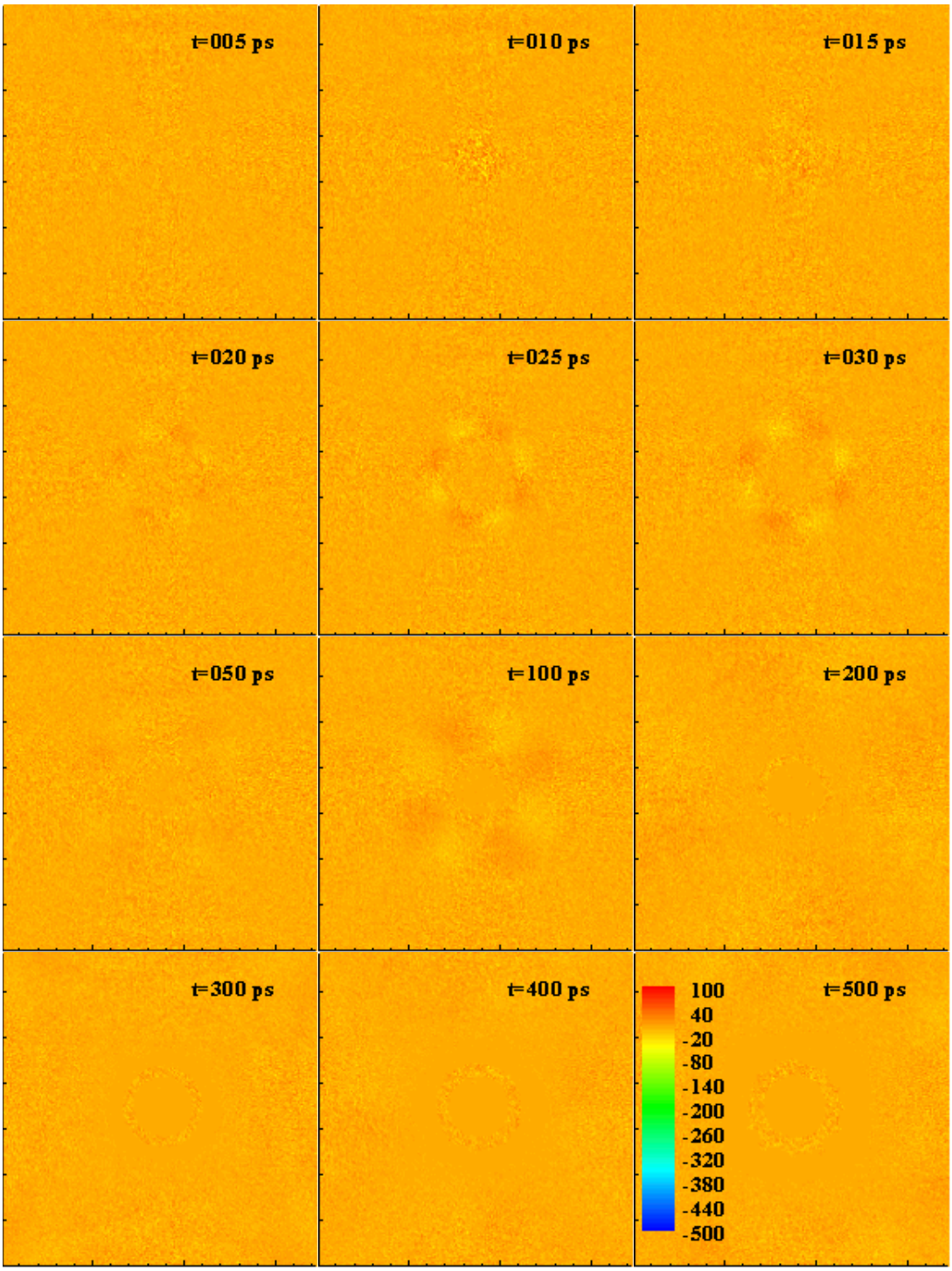

Figure 11. The stress $\sigma_{r\theta}$ (MPa) in an x (horizontal: 0–350 nm)–y (vertical: 0–350 nm) plane 1.71 nm thick centred at $z = 245.34$ nm.

cell 1 with a factor χ

$$\chi = \left[1 + \left\{[\delta E_1]\left[\frac{1}{2}\sum_{i=1}^{N} m_i \cdot [(v_{i,1} - \bar{v}_1)^2 + (v_{i,2} - \bar{v}_2)^2 + (v_{i,3} - \bar{v}_3)^2]\right]^{-1}\right\}\right]^{1/2}, \quad (5)$$

where $v_{i,j}$ and $\bar{v}_j$ ($j = 1, 2, 3$) are the velocities of atom i and the average velocity in the x, y and z directions for atoms within cell 1. N is the number of atoms within the cell. The new velocity $v'_{i,j}$ of atom i is calculated as

$$v'_{i,j} = (v_{i,j} - \bar{v}_j) \cdot \chi + \bar{v}_j \qquad j = 1, 2, 3. \quad (6)$$

The above velocity scaling ensures that the total momentum of the atoms within cell 1 is conserved and only the thermal (random) movement is scaled.

After the laser energy absorption in cell 1, the incident laser energy on cell 2 will be $E_2 = E_1 - \delta E_1$. Then, the

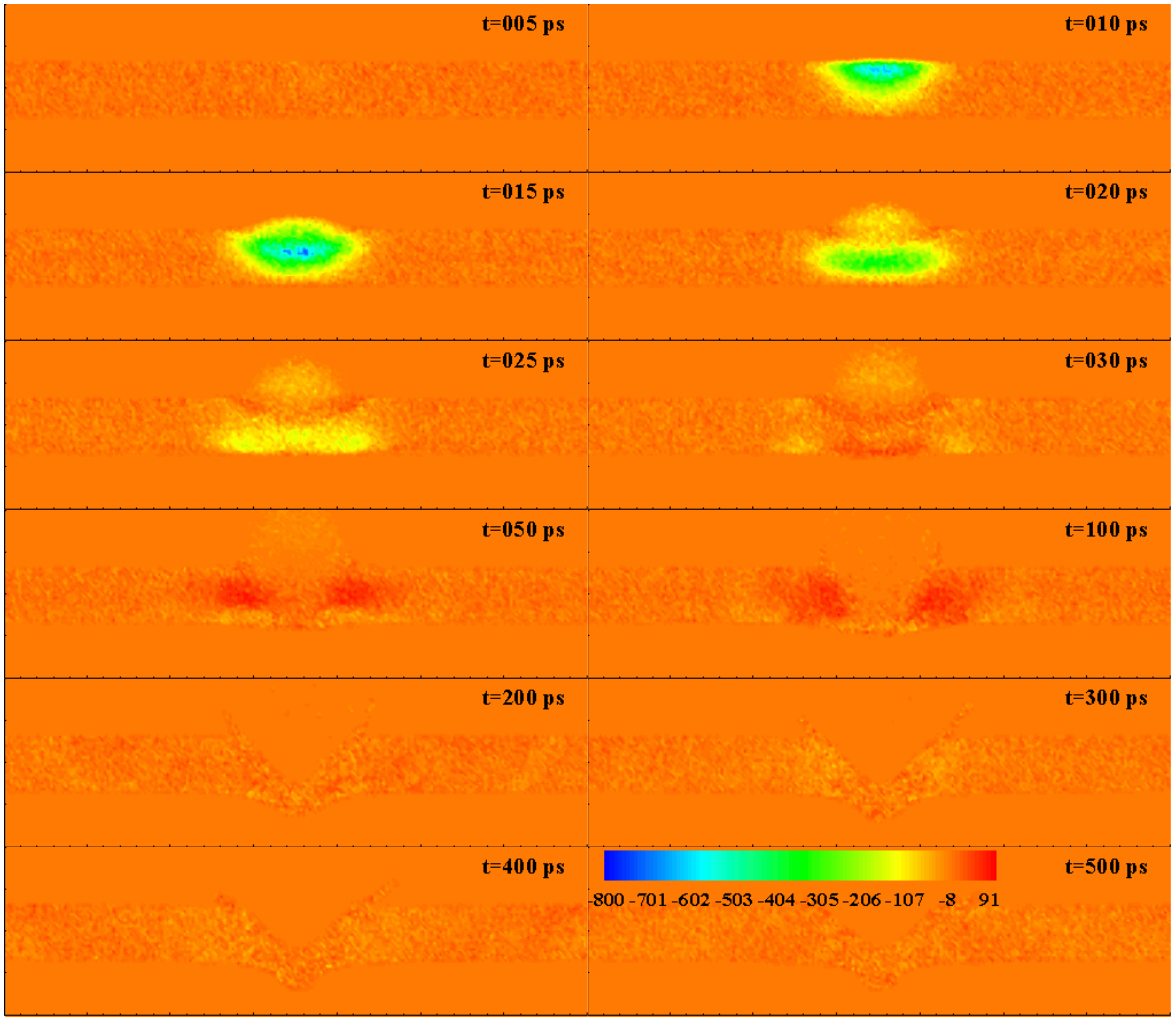

Figure 12. The stress σ_{rr} in an x (horizontal: 0–350 nm)–z (vertical: 180–280 nm) plane 1.77 nm thick centred at $y = 174.53$ nm.

aforementioned procedure can be applied to calculate the laser beam absorption in cell 2. The same laser beam absorption treatment is applied to cells in other areas of the MD domain.

3. Results and discussion

In the sections that follow, first of all, we will discuss the results for a sample of 648 fcc unit cells (350.83 nm) in the x and y directions, and 60 fcc unit cells (32.48 nm) in the z direction. The pulse energy is taken as 1.6×10^{-14} J, which corresponds to an energy density level of 100 MW cm^{-2}. As indicated in table 1, the spatial distribution of the laser pulse is assumed to have a radius of 25 nm at e^{-1} of the peak intensity. Before applying laser heating, the simulation is run for 100 ps (4000 steps), during which the velocity of atoms is scaled to make the sample reach 50 K gradually. Although, initially, the atom velocity is assigned to give a system temperature of 50 K, the potential energy is not the minimum. This 4000-step thermal equilibrium calculation is to ensure the system reaches minimum potential energy and thermal equilibrium. After this velocity scaling, the sample is simulated for another 100 ps (4000 steps) to eliminate the disturbance introduced by the velocity scaling. Periodic boundary conditions are applied to the boundaries in the x and y directions, and free boundary conditions to the boundaries in the z direction. Free spaces are added below and above the sample to capture the movement of atoms escaping from the sample. The computational domain measures 350.83 nm in the x and y directions, and 759.10 nm in the z direction with the back of the sample located at 213.71 nm. A total of 100 776 960 atoms are simulated for this case. A result comparison will be performed and discussed later for a sample consisting of 201 553 920 atoms.

3.1. Thermal transport and phase change

Figure 3 presents the velocity distribution of atoms within a domain of 1.77 nm size at 5 and 15 ps. It is evident that before the last heating ($t = 5$ ps), the velocity distribution follows Maxwell's distribution. Just after laser heating, there is a remarkable deviation of the velocity distribution from Maxwell's distribution, indicating that thermal equilibrium cannot be established. For purposes of comparison, we also show the velocity distribution within a domain far from the laser heating region (figure 3(*c*)). It is clear that in this region, the thermal equilibrium is preserved. Another possible reason for the non-equilibrium velocity distribution shown in figure 3(*b*) is the small number of atoms (69) in the domain,

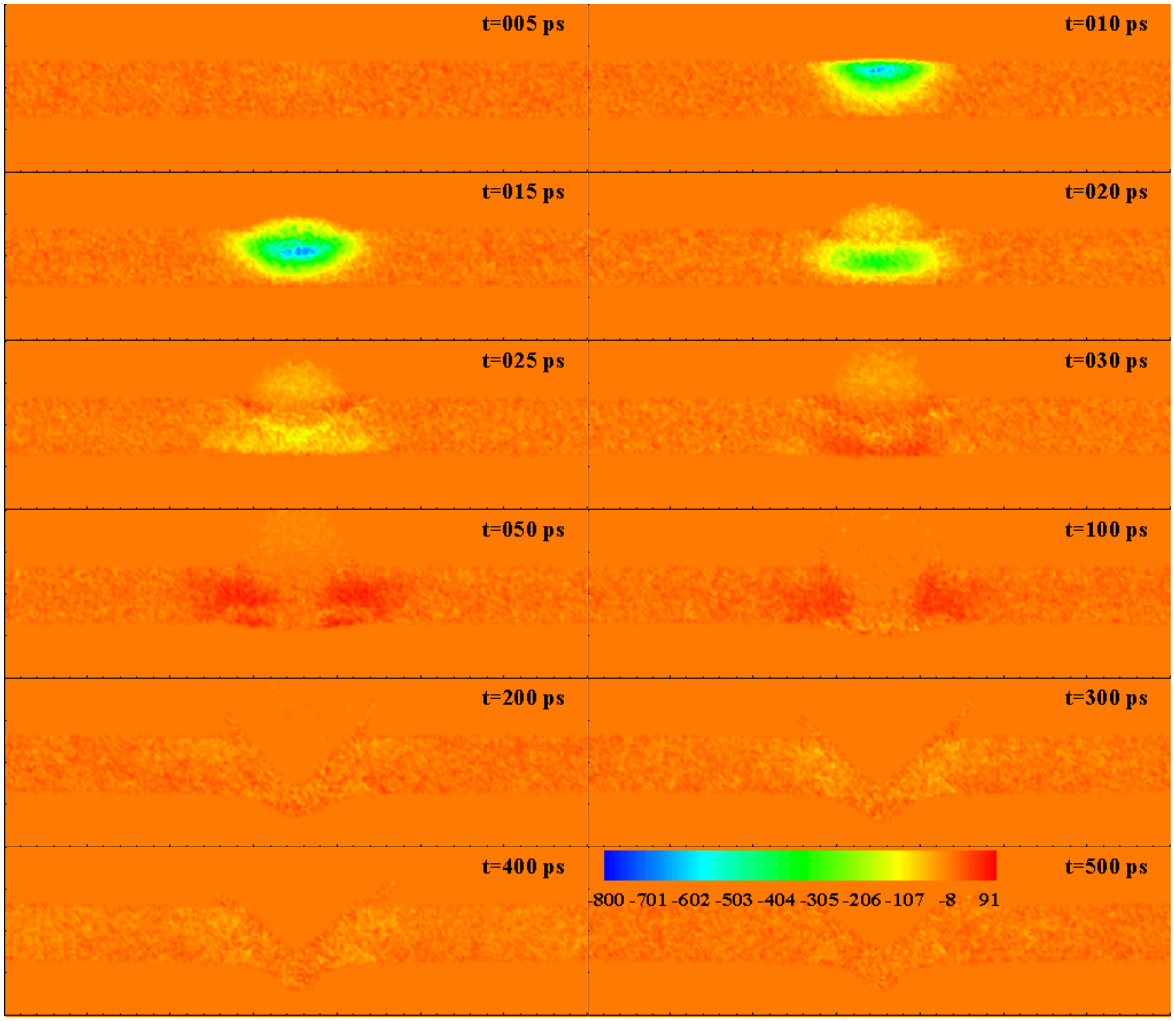

Figure 13. The stress $\sigma_{\theta\theta}$ in an x (horizontal: 0–350 nm)–z (vertical: 180–280 nm) plane 1.77 nm thick centred at $y = 174.53$ nm.

which is much smaller than those in figure 3(*a*) (137) and figure 3(*c*) (118). To further analyse this possible reason, we calculate the velocity distribution of a larger domain before and just after laser heating, as shown in figure 4. Figure 4(*a*) (the domain has 499 atoms) shows the velocity distribution before laser heating ($t = 5$ ps), which is close to that shown in figure 3(*a*). Figure 4(*b*) (the domain has 268 atoms) shows the velocity distribution just after laser heating. It is obvious that with a larger number of atoms under consideration, the velocity distribution shown in figure 4(*b*) is closer to the Maxwell's distribution than that in figure 3(*b*). On the other hand, figure 4(*b*) still shows appreciable deviations from the Maxwell distribution, indicating that the picosecond laser heating introduces strong disturbance to the thermal equilibrium. In this work, the temperature T of the sample is still calculated following the traditional definition

$$\frac{3}{2}k_{\mathrm{B}}T = \frac{1}{N}\sum_{i}\frac{1}{2}m_i v_i^2, \tag{7}$$

where k_{B} is the Boltzmann's constant and v_i is the velocity of the atom. It needs to be pointed out that this temperature is used only to reflect the average kinetic energy of atoms. Figure 5 shows the temperature evolution in an x–z plane located at $y = 174.53$ nm, which is close to the centre of the target in the y direction. At 15 ps (at the end of the laser pulse) a temperature as high as 500 K is observed at the top centre of the sample. From the beginning to 20 ps, the top centre of the sample experiences a thermal expansion. Then, an explosion takes place, which is accompanied by rapid cooling. A hole is formed after atoms move out of the sample. At the surface of the hole, the temperature reduces to about 100 K. To provide a clear idea of the heating and cooling processes, the evolution of the average kinetic energy of atoms originally located in the top centre ($x = 175.414$ nm, $y = 175.414$ nm and $z = 244.057$ nm) of the sample is plotted in figure 6. The kinetic energy is normalized by dividing it by k_{B} and is in the unit of Kelvin. It is found that the kinetic energy reaches the maximum value of 1500 K at 15 ps. At 500 ps, the kinetic energy becomes about 900 K, showing a decay of 40% from the maximum value.

In order to remove one electron from the argon atom to ionize it, the required energy (ionization energy) is 15.76 eV [55]. The densities of electrons (n_{e}), ions (n_{i}) and neutral atoms (n_{a}) are related to the temperature T as [56]

$$\frac{n_{\mathrm{e}}n_{\mathrm{i}}}{n_{\mathrm{a}}} = \frac{2U_{\mathrm{i}}}{U_{\mathrm{a}}}\left(\frac{2\pi m_{\mathrm{e}}k_{\mathrm{B}}T}{h^2}\right)^{3/2}\exp\left(\frac{-\chi}{k_{\mathrm{B}}T}\right), \tag{8}$$

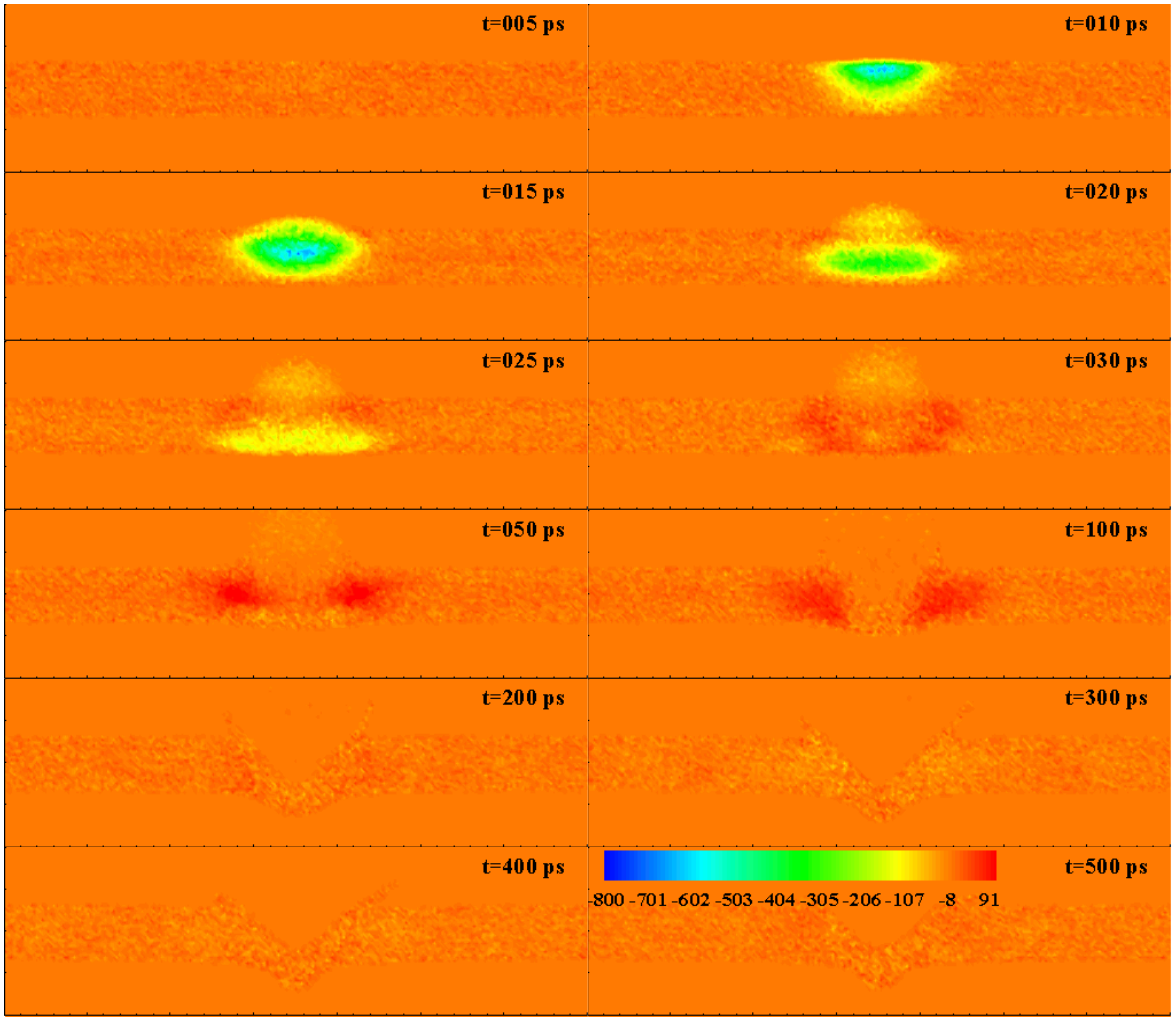

Figure 14. The stress σ_{zz} in an x (horizontal: 0–350 nm)–z (vertical: 180–280 nm) plane 1.77 nm thick centred at y=174.53 nm.

where U_i and U_a are the partition functions for singly ionized and neutral atoms, respectively. The partition function is an average value of the degeneracy over all states, weighted according to their populations. m_e is the mass of electrons, h is Planck's constant and χ is the ionization energy. For the highest temperature (∼500 K) observed in this computation, $k_B T$ is only about 2.74×10^{-3} eV, much smaller than the ionization energy. Therefore, plasma generation can be neglected in this work. In the laser–material interaction studied in this work, the atomic electrons will change their energy due to laser beam absorption. Due to the weak plasma generation involved in the process, the change in the electronic energy will not have a significant effect on the overall energy absorption for increasing the kinetic and potential energies of atoms.

Figure 7 presents the evolution of the temperature in an x–y plane of 1.71 nm thickness located at $z = 245.34$ nm (surface of the sample). It is evident that from 50 ps, the centre of the plane becomes loose, and atoms start to separate from each other. At 200 ps, a clear hole has formed. Then, an empty region starts to emerge around the outside of the hole. The ring observed at 500 ps is the protrusion observed in figure 5. The empty region observed in figure 7 has been marked in figure 5 as well. During laser heating, a large number of atoms are ejected from the sample surface. Due to momentum conservation, the laser-heated region moves in the other direction ($-z$). This movement drags the region adjacent to the hole to move in the negative z direction, thereby resulting in a slight displacement of this region in the negative z direction. On a closer look at figure 5 at 400 ps, it can be observed that the empty region has a small shift in the vertical direction, making this region a little lower than the rest of the sample surface. This small displacement is responsible for the empty region at the outside of the hole. It is evident that this empty region is not circular in shape, meaning the finite size of the sample has strong boundary effects on nanomanufacturing. In addition, pronounced irregularities are observed adjacent to the protrusion. The possible reason for these irregularities is the non-equilibrium movement of atoms. In a nanodomain, atoms will show strong statistical uncertainty in terms of thermal movements. The initial non-uniform thermal movement will strongly influence the movement of atoms, resulting in the non-uniformity of the protrusion.

3.2. Stress development and propagation

In order to suppress the statistical uncertainty, the local stress is averaged over a small domain with a size of about 1.7 nm.

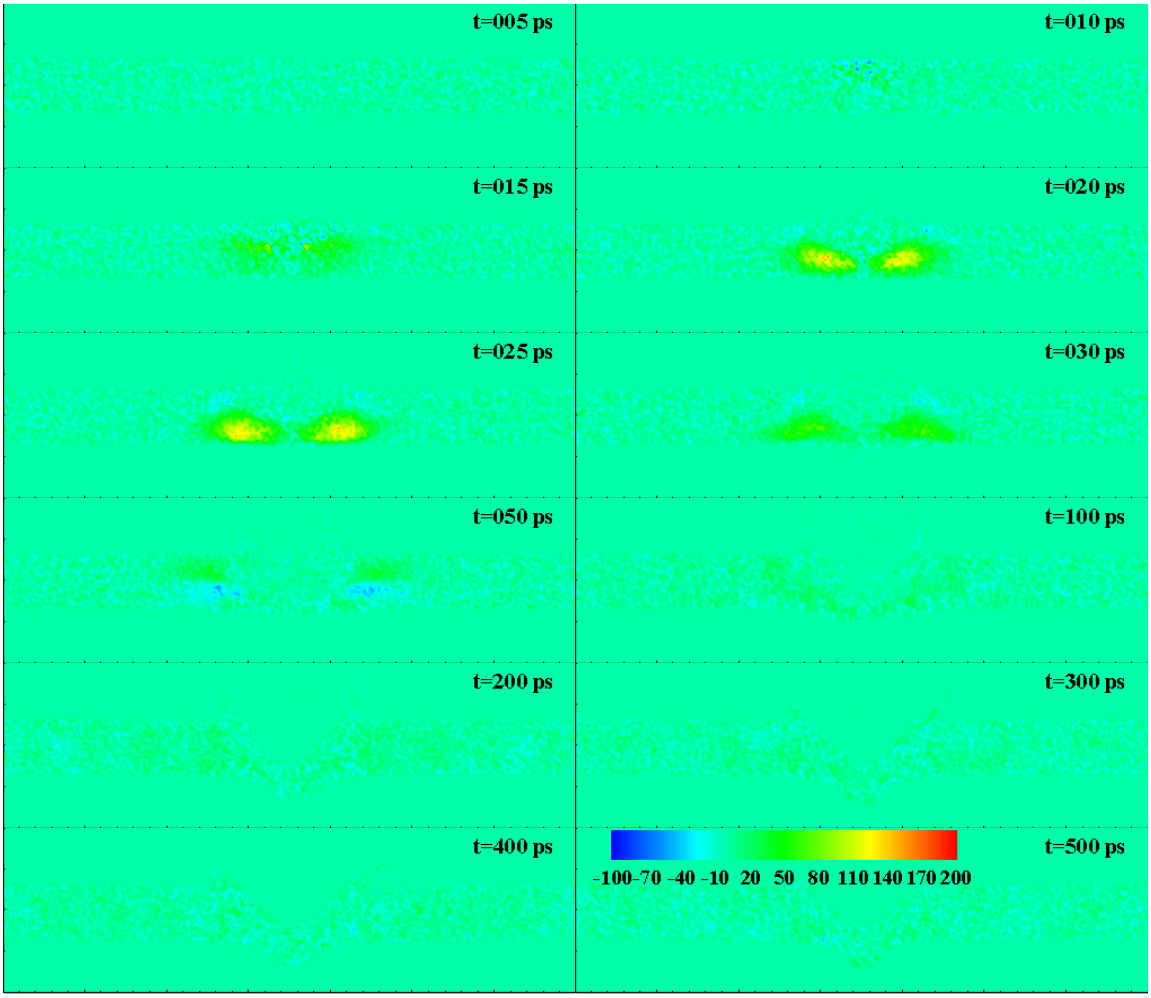

Figure 15. The stress σ_{rz} in an x (horizontal: 0–350 nm)–z (vertical: 180–280 nm) plane 1.77 nm thick centred at $y = 174.53$ nm.

The averaged stress is calculated as [48]

$$\sigma_{mn} = -\frac{1}{\Delta V}\left(\sum_{i\neq j}^{N} r_{ij,m} F_{ij,n} + \delta_{mn} \cdot N k_{\mathrm{B}} T\right), \qquad (9)$$

where ΔV is the volume of the small domain, and $Nk_{\mathrm{B}}T$ is the stress induced by the movement of atoms. In our work [48], equation (9) yielded a smooth stress calculation. The laser beam is axis symmetric; therefore, the stress calculated using equation (9) is transformed to cylindrical coordinates. Figures 8–11 present the evolution of stresses σ_{rr}, $\sigma_{\theta\theta}$, σ_{zz} and $\sigma_{r\theta}$ in an x–y plane 1.71 nm thick located at $z = 245.34$ nm (the top surface of the sample). In x–y planes, shear stresses $\sigma_{\theta z}$ and σ_{rz} are very weak and are not presented in this work.

In figure 8 it is evident that during laser heating (0–15 ps), a strong compressive stress develops in the heating region due to the substantial thermal expansion. The compressive stress could be as strong as 400 MPa. At the end of the laser pulse, a tensile stress is observed behind the compressive stress, which is propagating outside. The tensile stress is much weaker and is of the order of 50 MPa. Although the stress distribution in space is axis symmetric initially, it becomes discontinuous in space and does not follow the circular shape when it propagates out (50 and 100 ps). This is because the sample is crystalline and anisotropic in space. The x and y directions are the [100] direction and the directions towards the four angles are the [110] direction. For an argon crystal at 50 K, the stress wave travels at a speed of 1425 m s^{-1} in the [100] direction and 1500 m s^{-1} in the [110] direction [57]. For this reason, the stress σ_{rr} does not follow the circular shape when it propagates out. When the stress wave reaches the boundary of the computational domain, it enters the domain from the opposite boundary because of the periodical boundary conditions in the x and y directions. This makes the stress distribution more complicated as shown in figure 8 after 200 ps.

In contrast to σ_{rr}, the normal stress $\sigma_{\theta\theta}$ shows little visible propagation in space (figure 9). It is understandable that since the stress $\sigma_{\theta\theta}$ will propagate in the θ direction predominantly, its propagation in other directions will be relatively weak. During laser heating, the stress is dominated by a compressive stress as high as 400 MPa. For the normal stress σ_{zz}, its propagation is largely along the z direction. Therefore, no propagation of σ_{zz} in the x and y directions is observed in figure 10. σ_{zz} is featured with a compressive stress in the centre and a tensile stress at the edge. It is found that the location of the tensile stress corresponds to the location of the protrusion (the ring) around the hole observed at 300 ps. It suggests that the compressive stress in the centre pushes the material out to

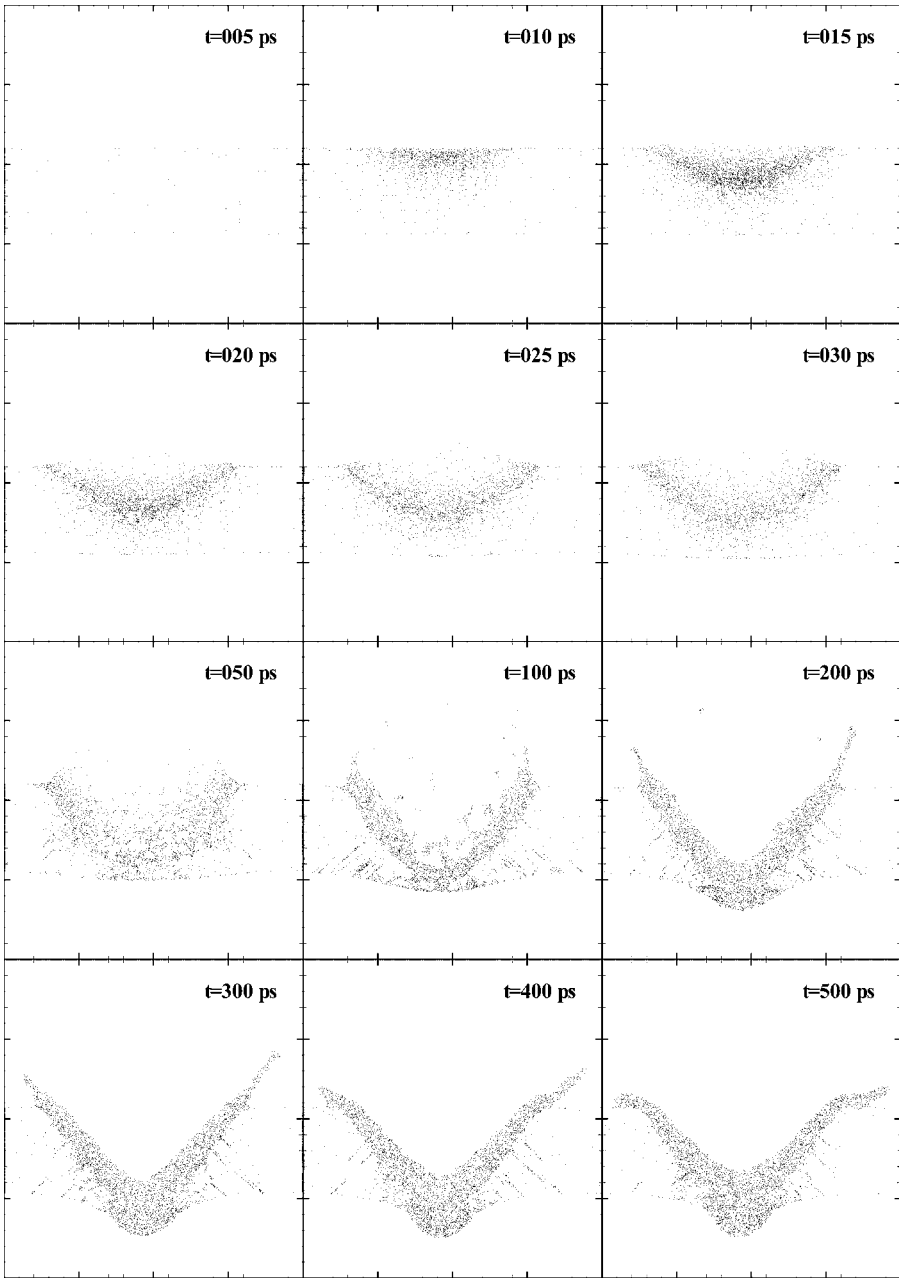

Figure 16. Snapshots of atomic positions in an x (horizontal: 120–240 nm)–z (vertical: 180–300 nm) plane 1.77 nm thick centred at $y = 174.53$ nm.

form the hole while the tensile stress around the edge pulls the material to form the protrusion. The shear stress $\sigma_{r\theta}$ (figure 11) is weak during laser heating, and is only visible at the end of the laser pulse (20 ps). The magnitude of the shear stress ($\sim$30 MPa) is much smaller than that of the normal stresses discussed above.

Figures 12–14 delineate the development and propagation of normal stresses σ_{rr}, $\sigma_{\theta\theta}$ and σ_{zz} in an x–z plane 1.77 nm thick centred at $y = 174.53$ nm, which is almost the central plane in the y direction. It is observed that upon laser irradiation, very strong compressive normal stresses developed just beneath the sample surface ($t = 10$, 15 and 20 ps in figures 12–14). These normal stresses are of the order of 700 MPa initially. It is these stresses that push the material to explode out from the sample surface. This phenomenon, namely phase explosion, features a mixture of liquid and vapour ejecting from the sample [58, 59]. After phase explosion, these normal stresses quickly reduce to the order of 100 MPa. In addition, these normal stresses propagate to the bottom of the sample, and are then reflected back. This propagation and reflection is more obvious for thicker samples, as detailed in our recent work [54]. After reflection, the compressive stresses become tensile stresses and reach the surface of the sample. The propagation of these normal stresses is not exclusively along the z direction. Therefore, after reflection they split into two parts separated from each other. These tensile normal stresses have strong effects on the formation of the nanohole (discussed later). At 20, 25 and 30 ps, it can be seen from figures 12–14 that the

vapour/melt ejected from the sample surface has a very high compressive stress of the order of hundreds of MPa, which means very high pressure in this mixture. Due to this high pressure, the mixture quickly expands in space, which can be observed at 50 and 100 ps. Since the x–z plane of interest is almost the central plane in the y direction, shear stresses $\sigma_{\theta z}$ and $\sigma_{r\theta}$ are nearly zero because of the symmetry with respect to this plane. For this reason, only the shear stress σ_{rz} is shown in figure 15. The shear stress σ_{rz} is becoming stronger when it propagates towards the bottom of the sample, which is indicated by the growing green and yellow regions from 10 to 25 ps. At 50 ps, this shear stress changes direction after reflection, which is demonstrated by the change in colour from green to blue. At 100 ps, this shear stress becomes much weaker. This is probably because when the reflected shear stress reaches the solid–liquid interface, part of it penetrates into the liquid and is dissipated by the liquid substantially.

In the simulations conducted in this work, free boundary conditions are applied to the z directions. This introduces stress wave reflections at the z boundaries that have been studied in our previous work [51]. It was recognized these undesired boundary stress reflections can affect the evolution of the surface structure and alter the final surface profile [60]. The periodic boundary conditions applied to the x and y directions allow the stress waves travelling out of the computational domain to re-enter the domain, which is not physically reasonable for practical laser-assisted nanomanufacturing. Boundary conditions that can absorb the incident stress waves and eliminate the undesired reflections are expected to improve the result. Moseler *et al* [60] have developed a method to drastically reduce the amplitude of the reflected wave. In the laser-assisted surface nanostructuring that is studied in this work, the boundary region can experience substantial deformation and phase change. The method developed by Moseler *et al* [60] provides a sound approach to further boundary condition design to accommodate the boundary deformation and phase change and to reduce boundary stress wave reflection.

3.3. Nanoscale surface structure and sub-surface structural damage

Figure 16 presents snapshots of atomic positions in an x–z plane 1.77 nm thick centred at $y = 174.53$ nm. In these plots, each dot represents an atom. At 5 ps, laser heating is weak, and the sample shows a uniform structure. At 10 ps, the centre at the surface becomes dark because the local solid has been melted. The random distribution of atoms in this region makes it look dark. At 15 ps, vapour is observed at the surface of the central part of the sample. At 50 ps, the melt in the sample experiences intense phase explosion. A large number of nano-droplets are formed and ejected from the sample. At the same time, a liquid layer of about 10 nm thickness is attached to the surface of the hole. Because of phase explosion, part of the liquid layer is driven by the pressure to move out of the hole to form a protrusion at the edge (200–500 ps). It is important to note that starting from 50 ps, tilted dark lines are observed in the region adjacent to the bottom of the sample. These dark lines mean that the local material has been destroyed. Normal and shear

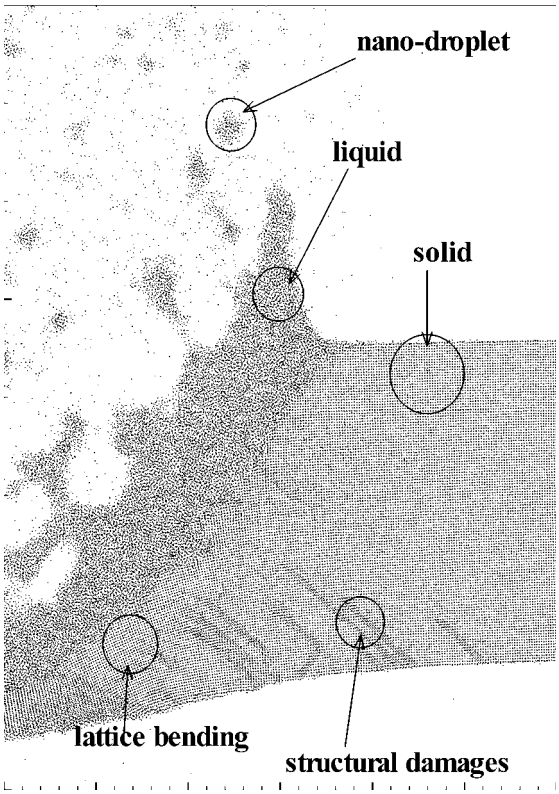

Figure 17. Detailed atomic positions at $t = 100$ ps in an x (horizontal: 180–240 nm)–z (vertical: 200–280 nm) plane 1.77 nm thick centred at $y = 174.53$ nm.

stresses play important roles in inducing the structural damage. For example, when the strong compressive normal stress is reflected at the bottom of the sample, it becomes tensile. This strong tensile stress could tear the material apart, resulting in structural damages. It is observed that these dark lines approximately follow 45° with respect to the z axis. This is because, in this direction, the shear stress induced by the normal stress σ_{zz} has the maximum value. It is interesting to note that these sub-surface structural damages experience some formation and disappearing procedures, and not all of them are permanent. For instance, comparing the plots at 100 and 400 ps reveals that some dark lines formed at 100 ps are close to the bottom of the sample and do not exist anymore at 400 ps. This phenomenon will be discussed in more detail for the larger sample under surface nanostructuring.

Figure 17 displays detailed positions of atoms in an x–z plane at 100 ps. As marked in the figure, the solid region shows a regular lattice structure. In the liquid region, atoms are randomly distributed in space. Nano-droplets of 3–4 nm diameter or smaller are observed. When phase explosion occurs, attributed to momentum conservation, the lower part of the sample moves in the opposite z direction. Because of this movement, the lattice structure is bent, which is marked in the figure. For the dark lines observed in figure 16 (the structural destruction), figure 17 shows that in these regions atoms are dislocated and the regular lattice structure no longer exists. We have studied the status of thermal equilibrium in the region experiencing structural destruction. The velocity distribution is calculated and compared with the Maxwell distribution. It is

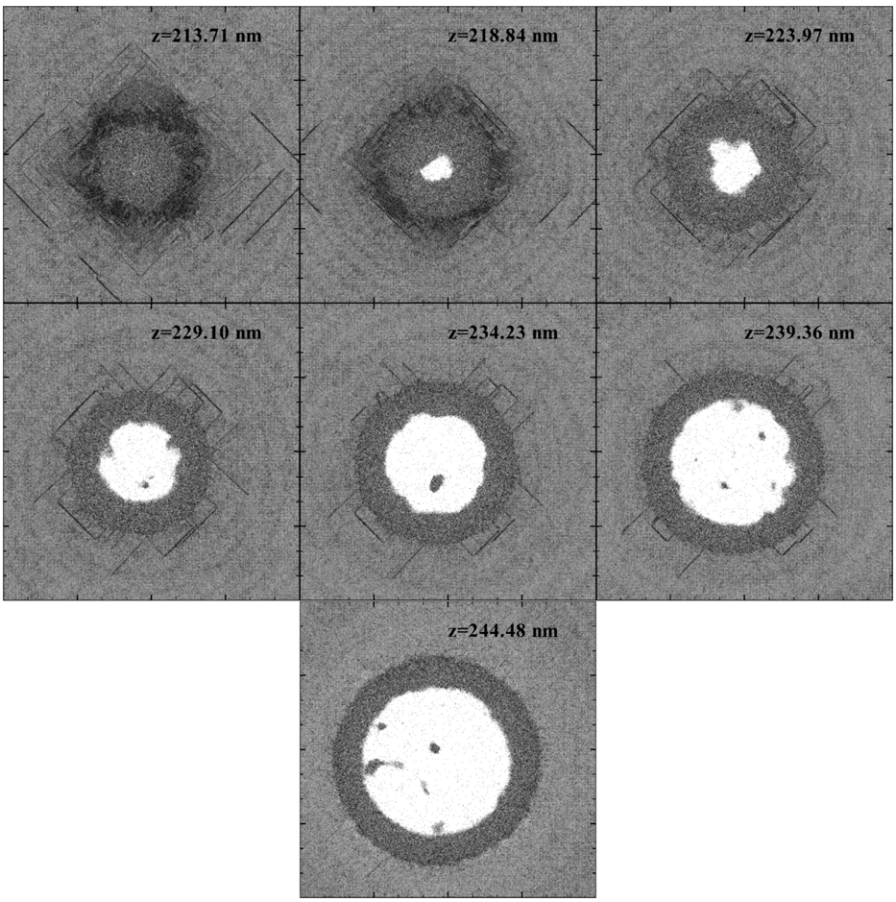

Figure 18. Structural damage in x (horizontal: 120–240 nm)–y (vertical: 120–240 nm) planes at different z locations at 200 ps. The plane with $z = 213.71$ is close to the bottom of the sample and the one with $z = 244.48$ nm is near the top of the sample.

found that the structural destruction does not introduce tangible disturbance in the local status of thermal equilibrium.

In order to have a clear idea about the distribution of structural damage in space, we plot them in x–y planes (the plane normal to the laser incident direction) of different z locations at 200 ps (figure 18). The thickness of each plane is 1.71 nm. The weak circular rings in the plots are induced by stress wave propagation, which leads to a slight displacement of atoms in space. It is observed that structural damages (dark straight lines) follow 45° with respect to either the x or y coordinate. This phenomenon could be attributed to the geometry of the sample. As we discussed before, when the stress wave reaches one boundary of the sample, it will re-enter the sample from the opposite boundary due to the periodic boundary conditions applied to the x and y directions. The re-entering stress wave can strongly interfere with the original one and change the pattern of the stress distribution in space. This phenomenon is also strongly affected by the geometry of the sample. In this work, the x and y coordinates follow the [100] direction of the crystal. Following the direction of 45° with respect to the x or y coordinate, the shear stress is normal to the connection between the closest atomic pairs, meaning that the shear stress does not need to overcome the strongest atomic force (the force between the closest atomic pairs) to induce atom shifts in space. This will give one possible explanation as to why the structural damages follow the direction of 45° with respect to the x or y coordinate. At $z = 213.71$ and 218.84 nm, in addition to the dark straight lines, black clouds are observed around the circular grey region in the centre. The circular grey region in the centre is the melted part while the black clouds mean that the material is still in solid state but with destroyed crystal structure.

In addition to the case detailed above, we also study the nanostructuring of the same sample as the one discussed above, but with a smaller pulse energy of 8×10^{-15} J. Figure 19 displays the snapshots of atomic positions at different times. Before 30 ps, the target shows behaviour similar to that presented in figure 16. Starting from 50 ps, the behaviour of the sample shows differences, especially in the formation and propagation of sub-surface structural damage. At 100 ps it is observed that many dark lines (sub-surface structural damages) are formed beneath the liquid layer of the nanohole. Similar to the dark lines observed in figure 16, these dark lines approximately follow the direction of 45° with respect to the z coordinate. However, at 200 ps, no dark lines exist any more, meaning the structural damage observed at 100 ps is temporary in nature. At 500 ps, the profile of the nanohole shows a regular structure, not like the one observed in figure 16. This could be due to the smaller laser pulse energy used in this case, which results in much less intense movement of atoms.

In order to attain more knowledge about the formation and propagation of the temporary and permanent sub-surface structural damages, we study a much larger sample under surface nanostructuring. This sample has 648 fcc cells in

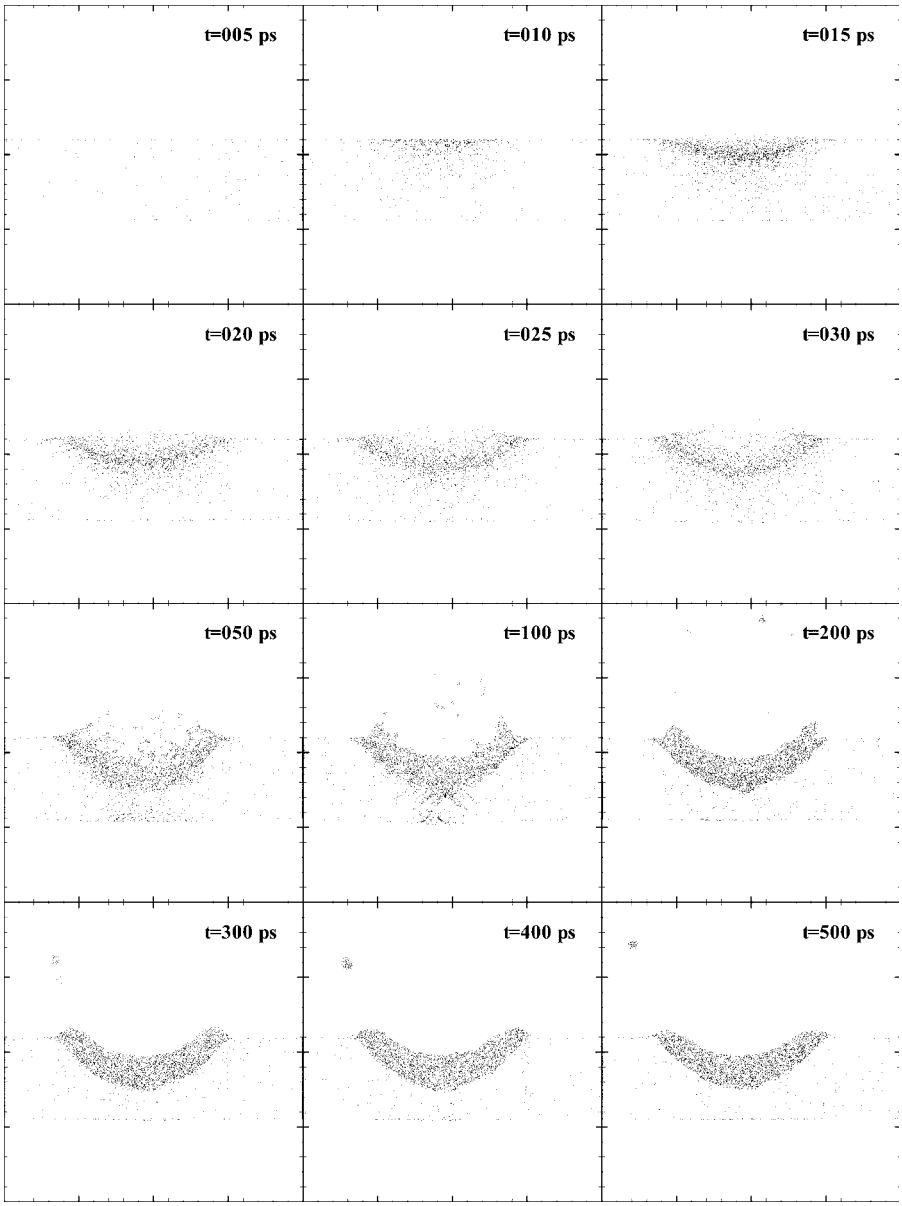

Figure 19. Snapshots of atomic positions in an x (horizontal: 120–240 nm)–z (vertical: 180–300 nm) plane 1.77 nm thick centred at $y = 174.53$ nm. Sample size: 350.83 nm × 350.83 nm × 32.48 nm ($x \times y \times z$); laser pulse energy: 8×10^{-15} J.

the x and y directions, and 120 fcc cells in the z directions. A total of 201 553 920 atoms are modelled. The laser beam follows the same temporal and spatial distribution described by equation (3) and has a pulse energy of 1.6×10^{-14} J. Snapshots of atomic positions at different times are displayed in figure 20. At 30 ps, a few tilted dark straight lines are observed beneath the nanohole and more are observed at 50 ps. Comparing the plots at 50 and 100 ps, it is evident that the straight dark lines move with time in space. At 200 ps, these dark lines disappear completely. From 200 to 500 ps, the long dark lines just beneath the nanohole always exist, meaning they are permanent in nature.

For the laser-assisted surface nanostructuring studied in this work, the sample material (argon) is chosen in order to keep the calculation simple. In addition, the optical field is constructed to simplify the situation while in experiments the laser beam has a much sharper distribution in space attributed to the optical field enhancing effect of the STM tip [61]. As a result, the thermal, mechanical and structural phenomena discussed in this work are qualitative rather than quantitative. In surface nanostructuring using laser-assisted STM, due to the extremely small domain under investigation, the dynamic processes including thermal evolution, stress formation and propagation, as well as structural damages have not been well addressed in experiments. Limited experimental data lead to difficulties in evaluating the reported physical processes in this work. In the work by Huang *et al* [62], protrusions were observed around the edge of nanoholes created using laser-assisted AFM. The profile of the protrusions is close to that shown in figures 16, 19 and 20. More advanced experimental and MD studies are needed to explore the physical processes involved in practical laser-assisted STM nanostructuring. Comparison of numerical and experimental results will lead to a deep understanding of the underlying

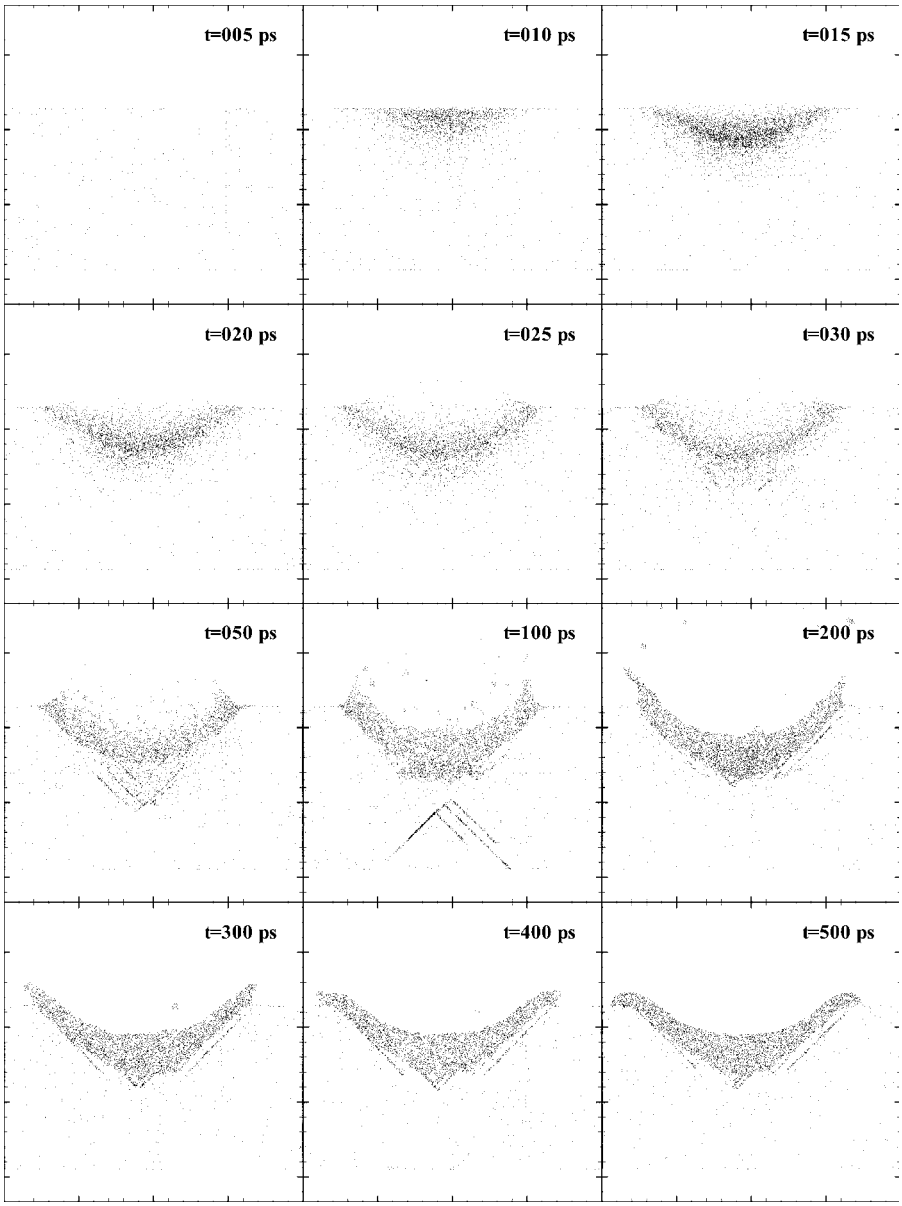

Figure 20. Snapshots of atomic positions in an x (horizontal: 120–240 nm)–z (vertical: 180–300 nm) plane 1.77 nm thick centred at $y = 174.53$ nm. Sample size: 350.83 nm × 350.83 nm × 64.97 nm ($x \times y \times z$), laser pulse energy: 1.6×10^{-14} J.

physics in surface nanostructuring with laser-assisted STM and help establish the building blocks of knowledge required for optimization and implementation of this technique.

4. Conclusion

In this work, large-scale parallel MD simulations were conducted to study the thermal and mechanical behaviour in surface nanostructuring with laser-assisted STM. More than 200 million atoms were tracked in the simulation. Protrusions with evident irregularities were observed at the edge of the hole when a large pulse energy was employed. Thermally induced instability played an important role in forming this structural irregularity. During laser heating, strong compressive stresses developed beneath the sample surface. It was these compressive stresses that drove atoms to move to induce phase explosion. In addition, the propagation of the stress in the sample was endowed with a strong anisotropic nature because of the direction-dependent stress wave speeds in the crystal. Visible sub-surface structural damages were observed in the direction of 45° with respect to the z-axis. The strong tensile stress resulting from the reflection of the compressive stress at the bottom played the most significant role in inducing the structural damage. By studying different conditions of surface nanostructuring, temporary and permanent sub-surface nanoscale structural damage was found. After formation, the temporary structural damage propagated in space and disappeared at the end.

Acknowledgments

Support for this work from NSF (CTS: 0210051, 0400458), Nebraska Research Initiative, and Sumitomo Foundation are gratefully acknowledged. The author thanks Dr Xianfan Xu

of Purdue University, Dr David A Willis of the Southern Methodist University and Cecil Lawrence and Zhanrong Zhong of UNL for their help during the preparation of this manuscript.

References

[1] Kuk Y, Becker R S, Silverman P J and Kochanski G P 1990 *Phys. Rev. Lett.* **64** 456–9
[2] Hamers R J and Markert K 1990 *Phys. Rev. Lett.* **64** 1051–4
[3] Amer N M, Skumanich A and Ripple D 1986 *Appl. Phys. Lett.* **49** 137–9
[4] Pfeiffer W, Sattler F, Vogler S and Gerber G 1997 *Appl. Phys.* B **64** 265–8
[5] Quate C F 1997 *Surf. Sci.* **386** 259–64
[6] Grafström S 2002 *J. Appl. Phys.* **91** 1717–53
[7] Jersch J, Demming F and Dickmann K 1997 *Appl. Phys.* A **64** 29–32
[8] Jersch J, Demming F, Fedotov I and Dickmann K 1999 *Appl. Phys.* A **68** 637–41
[9] Huber R, Koch M and Feldmann J 1998 *Appl. Phys. Lett.* **73** 2521–3
[10] Boneberg J, Münzer H-J, Tresp M, Ochmann M and Leiderer P 1998 *Appl. Phys.* A **67** 381–4
[11] Boneberg J, Tresp M, Ochmann M, Münzer H-J and Leiderer P 1998 *Appl. Phys.* A **66** 615–19
[12] Lu Y F, Mai Z H, Zheng Y W and Song W D 2000 *Appl. Phys. Lett.* **76** 1200–2
[13] Lu Y F, Hu B, Mai Z H, Wang W J, Chim W K and Chong T C 2001 *Japan. J. Appl. Phys.* **40** 4395–8
[14] Lu Y F, Mai Z H and Chim W K 1999 *Japan. J. Appl. Phys.* **38** 5910–15
[15] Jersch J and Dickmann K 1996 *Appl. Phys. Lett.* **68** 868–70
[16] Jersch J, Demming F, Hildenhagen L J and Dickmann K 1998 *Appl. Phys.* A **66** 29–34
[17] Lu Y F, Mai Z H, Qiu G and Chim W K 1999 *Appl. Phys. Lett.* **75** 2359–61
[18] Hu B, Lu Y F, Mai Z H, Song W D and Chim W K 2000 *1st Int. Symp. on Laser Precision Microfabrication* (*Omiya, Saitama, Japan*) pp 232–5
[19] Mai Z H, Lu Y F, Huang S M, Chim W K and Pan J S 2000 *J. Vac. Sci. Technol.* B **18** 1853–7
[20] Mai Z H, Lu Y F, Song W D and Chim W K 2000 *Appl. Surf. Sci.* **154–155** 360–4
[21] Chimmalgi A, Choi T and Grigoropoulos C P 2002 *ASME International Mechanical Engineering Congress and Exposition (New Orleans, LA)*
[22] Huang S M, Hong M H, Lu Y F, Lukỳanchuk B S, Song W D and Chong T C 2002 *J. Appl. Phys.* **91** 3268–74
[23] Lyubinetsky I, Dohnálek Z, Ukraintsev V A and Yates J T Jr 1997 *J. Appl. Phys.* **82** 4115–17
[24] Demming F, Dickmann K and Jersch J 1998 *Rev. Sci. Instrum.* **69** 2406–8
[25] Jersch J, Demming F, Fedotov I and Dickmann K 1999 *Rev. Sci. Instrum.* **70** 3173–6
[26] Dohnálek Z, Lyubinetsky I and Yates J T Jr 1997 *J. Vac. Sci. Technol.* A **15** 1488–92
[27] Ukraintsev V A and Yates J T Jr 1996 *J. Appl. Phys.* **80** 2561–71
[28] Yau S-T, Saltz D and Nayfeh M H 1990 *Appl. Phys. Lett.* **57** 2913–15
[29] Yau S-T, Saltz D and Nayfeh M H 1991 *J. Vac. Sci. Technol.* B **9** 1371–5
[30] Denk W and Pohl D W 1991 *J. Vac. Sci. Technol.* B **9** 510–13
[31] Martin O J F, Girard C and Dereux A 1995 *Phys. Rev. Lett.* **74** 526–9
[32] Madrazo A, Nieto-Vesperinas M and García N 1996 *Phys. Rev.* B **53** 3654–7
[33] Martin O J F and Girard C 1997 *Appl. Phys. Lett.* **70** 705–7
[34] Demming F, Jersch J, Dickmann K and Geshev P I 1998 *Appl. Phys.* B **66** 593–8
[35] Geshev P I, Demming F, Jersch J and Dickmann K 2000 *Appl. Phys.* B **70** 91–7
[36] Geshev P I, Demming F, Jersch J and Dickmann K 2000 *Thin Solid Films* **368** 156–62
[37] Shibahara M and Kotake S 1997 *Int. J. Heat Mass Transfer* **40** 3209–22
[38] Shibahara M and Kotake S 1998 *Int. J. Heat Mass Transfer* **41** 839–49
[39] Häkkinen H and Landman U 1993 *Phys. Rev. Lett.* **71** 1023–6
[40] Kotake S and Kuroki M 1993 *Int. J. Heat Mass Transfer* **36** 2061–7
[41] Herrmann R F W, Gerlach J and Campbell E E B 1998 *Appl. Phys.* A **66** 35–42
[42] Zhigilei L V, Kodali P B S and Garrison J 1997 *J. Phys. Chem.* B **101** 2028–37
[43] Zhigilei L V, Kodali P B S and Garrison J 1998 *J. Phys. Chem.* B **102** 2845–53
[44] Zhigilei L V and Garrison B J 2000 *J. Appl. Phys.* **88** 1281–98
[45] Ohmura E, Fukumoto I and Miyamoto I 1999 *Proc. International Congress on Applications of Lasers and Electro-Optics (Laser Institute of America, Orlando)* pp 219–28
[46] Schäfer C, Urbassek H M and Zhigilei L V 2002 *Phys. Rev.* B **66** 1–8
[47] Ivanov D S and Zhigilei L V 2003 *Phys. Rev.* B **68** 1–22
[48] Wang X 2004 *J. Heat Transfer* **126** 355–64
[49] Etcheverry J I and Mesaros M 1999 *Phys. Rev.* B **60** 9430–4
[50] Wang X and Xu X 2002 *J. Heat Transfer* **124** 265–74
[51] Wang X and Xu X 2003 *Int. J. Heat Mass Transfer* **46** 45–53
[52] Wang X and Xu X 2003 *J. Heat Transfer* **125** 1147–55
[53] Allen M P and Tildesley D J 1987 *Computer Simulation of Liquids* (Oxford: Clarendon)
[54] Wang X and Lawrence C 2004 *The 37th AIAA Thermophysics Conf. (Portland, Oregon, June 28–July 1)*
[55] Kittel C 1976 *Introduction to Solid State Physics* 5th edn (New York: Wiley)
[56] Hughes T P 1975 *Plasmas and Laser Light* (England: Adam Hilger)
[57] Keeler G J and Batchelder D N 1970 *J. Phys. C: Solid State Phys.* **3** 510–22
[58] Kelly R and Miotello A 1996 *Appl. Surf. Sci.* **96–98** 205–15
[59] Song K H and Xu X 1998 *Appl. Surf. Sci.* **127** 111–16
[60] Moseler M, Nordiek J and Haberland H 1997 *Phys. Rev.* B **56** 15439–45
[61] Lu Y F, Mai Z H and Chim W K 1999 *Japan. J. Appl. Phys.* **38** 5910–15
[62] Huang S M, Hong M H, Lu Y F, Lukỳanchuk B S, Song W D and Chong T C 2002 *J. Appl. Phys.* **91** 3268–74